



**HAL**  
open science

# Nature-Inspired Helicoidal Nanocellulose-Based Multi-Compartment Assemblies with Tunable Chiroptical Properties

Randy Mujica, Anusree Augustine, Matthias Pauly, Yann Battie, Gero  
Decher, Vincent Le Houerou, Olivier Felix

► **To cite this version:**

Randy Mujica, Anusree Augustine, Matthias Pauly, Yann Battie, Gero Decher, et al.. Nature-Inspired Helicoidal Nanocellulose-Based Multi-Compartment Assemblies with Tunable Chiroptical Properties. *Advanced Materials*, In press, 10.1002/adma.202401742 . hal-04559898

**HAL Id: hal-04559898**

**<https://hal.science/hal-04559898>**

Submitted on 3 May 2024

**HAL** is a multi-disciplinary open access archive for the deposit and dissemination of scientific research documents, whether they are published or not. The documents may come from teaching and research institutions in France or abroad, or from public or private research centers.

L'archive ouverte pluridisciplinaire **HAL**, est destinée au dépôt et à la diffusion de documents scientifiques de niveau recherche, publiés ou non, émanant des établissements d'enseignement et de recherche français ou étrangers, des laboratoires publics ou privés.

# Nature-Inspired Helicoidal Nanocellulose-Based Multi-Compartment Assemblies with Tunable Chiroptical Properties

Randy Mujica, Anusree Augustine, Matthias Pauly, Yann Battie, Gero Decher,\*  
Vincent Le Houérou,\* and Olivier Felix\*

Cellulose-based nanocomposites are highly appealing for the development of next-generation sustainable functional materials. Although many advances have been made in this direction, the true potential of fibrillar nanocomposites has yet to be realized because available fabrication approaches are inadequate for achieving precise structural control at the sub-micrometer scale. Here a spray-assisted alignment methodology of cellulose nanofibrils is combined with the layer-by-layer assembly into an additive manufacturing process in which the alignment direction of each cellulose layer is rationally selected to achieve thin films with a helicoidal arrangement of the nanofibrils. The helicoidal structure of the films is verified by measuring the circular dichroism (CD) of the samples. The sign and position of the structural CD peak show that the handedness and the pitch of the chiral structures can be easily tuned by deliberately selecting simple parameters, such as the number of consecutive cellulose layers sprayed in the same direction, and the angle of rotation between successive stacks of layers. To the authors' knowledge, this approach is unique as it offers the possibility to prepare complex nanocomposite architectures with various nanoscale-controlled sub-structures from different anisometric objects, which is enabling novel designs of composite films with damage-resistant and/or optical filtering functionalities.

strongly inspired by the examples of natural materials such as bone, nacre, crustacean shells, or wood, whose physical properties are outstanding compared to those of their individual building blocks (proteins, polysaccharides, and biominerals).<sup>[1,2]</sup> The remarkable functional properties of these biological materials arise from the organization of their nanoscale building blocks into complex hierarchical structures.<sup>[3–5]</sup> One such morphology consists of fibrillar building blocks arranged parallel to each other in adjacent stacked planes whose preferred orientation is progressively rotated by a few degrees, forming an effective helicoidal stack of fibrils.<sup>[1,3,6,7]</sup> The organization of chitin or cellulose fibrils in such helicoidal arrangements (referred to as twisted plywood-like or Bouligand structure<sup>[8,9]</sup>) has been associated with mechanical<sup>[10–16]</sup> and optical<sup>[17–19]</sup> functionalities in several animal and plant tissues.

Notably, fibers, anisometric nano-objects, often display different refractive indices for light polarized along and across their long axes. Therefore, helicoidally

stacked microfibrils form multilayers with a refractive index that varies periodically in space. This arrangement acts as a photonic crystal giving rise to what is known as Bragg reflection,<sup>[20]</sup>

## 1. Introduction

The use of nanosized building blocks to create synthetic composite materials with improved properties and functions is

R. Mujica, A. Augustine, M. Pauly, G. Decher, V. L. Houérou, O. Felix  
 Université de Strasbourg  
 CNRS

Institut Charles Sadron UPR22  
 Strasbourg F-67000, France

E-mail: [decher@unistra.fr](mailto:decher@unistra.fr); [v.lehouerou@unistra.fr](mailto:v.lehouerou@unistra.fr);  
[olivier.felix@ics-cnrs.unistra.fr](mailto:olivier.felix@ics-cnrs.unistra.fr)

M. Pauly, G. Decher, O. Felix  
 International Center for Materials Nanoarchitectonics  
 Tsukuba, Ibaraki 305-0044, Japan

 The ORCID identification number(s) for the author(s) of this article can be found under <https://doi.org/10.1002/adma.202401742>

© 2024 The Authors. Advanced Materials published by Wiley-VCH GmbH. This is an open access article under the terms of the [Creative Commons Attribution](https://creativecommons.org/licenses/by/4.0/) License, which permits use, distribution and reproduction in any medium, provided the original work is properly cited.

DOI: 10.1002/adma.202401742

Y. Battie  
 Université de Lorraine  
 LCP-A2MC  
 Metz F-57078, France

G. Decher  
 International Center for Frontier Research in Chemistry  
 Strasbourg F-67083, France

V. L. Houérou  
 Université de Strasbourg  
 CNRS  
 ICube UMR 7357, Illkirch F-67412, France

i.e., when the periodic spacing defined by half the helicoidal pitch ( $P/2$ ) is comparable to the wavelength of visible light, a photonic bandgap is formed that causes light to be reflected in a particular wavelength range centered at a  $\lambda_{\text{max}}$  as determined by the Bragg–Snell law,<sup>[21]</sup> giving rise to structural coloration. Remarkable examples of this phenomenon are the fruits of *Pollia condensata* and *Margaritaria nobilis*, whose metallic appearance and strong iridescent blue coloration are associated with the Bouligand arrangement of cellulose microfibrils in their epidermal cell walls, as verified by electron microscopy.<sup>[22,23]</sup> Moreover, the helicoidal photonic structures show a preferential reflection of circularly polarized light (CPL) with the same chirality as that of the helicoidal structure, mostly left-handed (L-CPL).<sup>[24–28]</sup> Only very few examples of biological materials reflecting right-handed circularly polarized light (R-CPL) have been reported, including the exocuticle of the beetle *Chrysina resplendens*, which reflects both handedness simultaneously due to the inclusion of an anisotropic layer between two separate left-handed layers that acts as a half-wave retarder.<sup>[29]</sup> The latter example perfectly illustrates the engineering interest in finding effective and versatile ways to prepare synthetic materials with well-controlled internal microstructures.

Various bottom-up strategies, e.g., controlled twisted stacking,<sup>[30]</sup> Langmuir–Schäfer assembly,<sup>[31]</sup> 3D printing techniques,<sup>[32]</sup> and evaporation-induced-self-assembly (EISA),<sup>[33]</sup> have been developed over the last decade for the preparation of artificial chiral photonic structures and materials from individual molecular and nanoscale entities. Among promising chiroptical components, cellulose nanocrystals (CNC) are highly attractive candidates as they exhibit liquid crystalline behaviors above a certain critical concentration allowing the spontaneous formation of long-range self-assembled helicoidal structures with selective light reflection and circular dichroism (CD).<sup>[34]</sup>

Since the work of Revol et al.,<sup>[35,36]</sup> EISA has become the preferred method for fabricating functional materials with submicrometer chiral organizations.<sup>[37–42]</sup> The authors reported the retention of the chiral nematic organization of CNC suspensions in the solid films after evaporation of the solvent. Films prepared using this method display characteristics of a one-dimensional photonic crystal, exhibiting structural coloration and preferential reflection of left-handed circularly polarized light. The wavelength of the reflected color can be tailored by manipulating the helical pitch, which is achieved through changes in the suspension's ionic strength<sup>[43]</sup> or drying conditions,<sup>[44]</sup> as well as through the application of magnetic<sup>[45,46]</sup> and electric fields.<sup>[47]</sup> Additionally, the handedness of the reflected circularly polarized light has also been effectively manipulated by incorporating an anisotropic domain between the left-handed cholesteric layers, which acts as a half-wave retarder.<sup>[48,49]</sup> This is similar to the structure of the cuticle of the scarab beetle *Chrysina resplendens*. A limitation of the EISA approach is that multiple domains (tactoids) are typically obtained in CNC films due to the competition of surface and nematic energies to establish the final helicoidal structure.<sup>[50–52]</sup> Furthermore, the approach is restricted in its selection of building blocks and matrix materials, and it does not enable independent control over CNC alignment in each layer. The resulting pitch and related properties can only be tuned within a narrow range.

An alternative approach exhibiting immense potential for nanoarchitectonics is the layer-by-layer (LbL) assembly<sup>[53–55]</sup> of

multilayer thin films, owing to the combination of spontaneous self-assembly and stepwise directed assembly.<sup>[56–58]</sup> Recently, we introduced a grazing incidence spraying (GIS) approach for a colloidal dispersion of 1D nanostructures at a small angle ( $<20^\circ$ ) relative to the receiving surface. This method promotes effective in-plane alignment of nanofibrils parallel to the spraying direction.<sup>[59]</sup> The combination of the GIS methodology with the LbL assembly allowed for the build-up of nanocomposite thin films of silver nanowires<sup>[60]</sup> and cellulose nanofibrils<sup>[61]</sup> displaying highly anisotropic optical and mechanical properties respectively. Recently we prepared chiral Bouligand nanostructures exhibiting very strong chiroptical properties from nonchiral plasmonic nanowires and nanorods by applying this simple, versatile and efficient directed self-assembly method.<sup>[62]</sup> The GIS-LbL approach is thus unique as it offers the possibility to incorporate various sub-structures (helicoidal stacks with opposite handedness and/or different pitches, unidirectional or random segments) made of different anisometric nano-objects within the same film to tune the mechanical and optical properties of the material. None of the presently established nano-fabrication approaches offers a similar versatility for the construction of complex nanocomposite architectures.

Here, we propose to use this combination with cellulose nanofibers (CNF) (a promising green biomaterial)<sup>[63]</sup> as a versatile additive manufacturing process in which the direction of alignment of the anisotropic reinforcing agent can be rationally designed to obtain thin-film materials with a complex internal structure. CNF were selected as model building blocks for the present work because they form reasonably robust LbL-films and because, in contrast to CNC,<sup>[34]</sup> CNF do not show any liquid crystalline behavior and thus cannot spontaneously self-assemble in helicoidal architectures. We therefore employ our directed assembly approach to fabricate composite films of CNF and poly(vinyl amine) (PVAm) possessing a controlled helicoidal arrangement of the nanofibrils. Left- and right-handed helices were fabricated with a uniform thickness and different pitches and number of turns. The resulting structures were analyzed using ellipsometry, scanning electron microscopy (SEM), UV–Vis spectroscopy, Mueller matrix spectroscopic ellipsometry (MMSE) and circular dichroism to determine their build-up, thickness, transparency, and chiroptical properties.

## 2. Results and Discussion

### 2.1. Fabrication of Helicoidally Reinforced CNF-Based Films

The proposed concept for preparing cellulose films with controlled helical structures is based on the assumption that the cellulose nanofibrils in each layer can be aligned independently. However, the orientation of an already deposited CNF layer might affect (or even prevent) the alignment of a new layer spray-deposited on top of it in a different direction. The two extreme cases would be the spraying of successive cellulose layers in parallel and perpendicular directions to each other, respectively.

In previous work, we have demonstrated the preservation of the parallel orientation of CNF in thin GIS-LbL films using cross-polarized microscopy, ellipsometry,<sup>[59]</sup> and Mueller matrix polarimetry.<sup>[64]</sup> Therefore, here we investigated the orientation

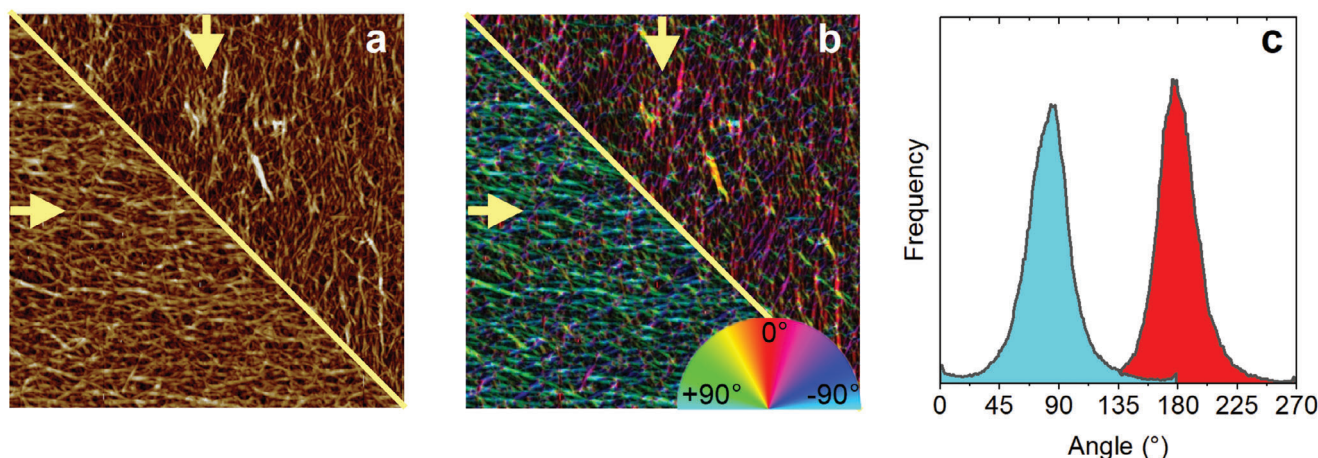


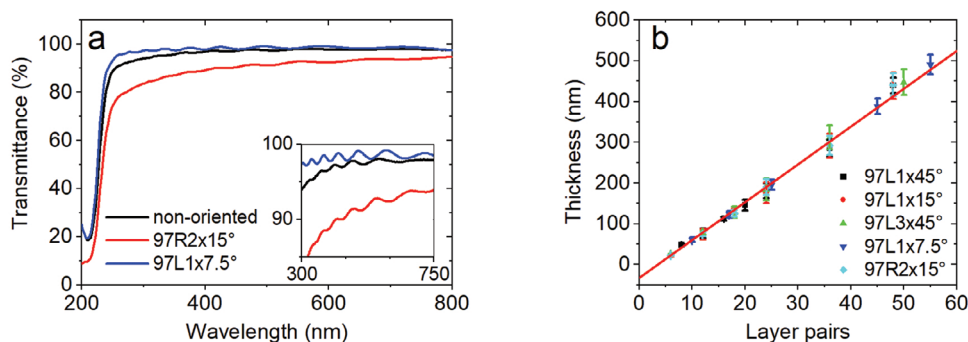
**Figure 1.** a) Superposition of representative AFM images of a PEI/CNF/PVAm/CNF film in which the CNF layers are sprayed in a perpendicular direction to each other. The vertical arrow indicates the spraying direction of the first layer and the horizontal one, the spraying direction of the second layer. The image size is  $2 \times 2 \mu\text{m}^2$ . b) AFM image in (a) color-coded according to the local orientation around each pixel. c) Orientation distribution of CNFs in the first (red) and second (blue) layers.

of two consecutive CNF layers sprayed in perpendicular directions to each other on a poly(ethyleneimine) (PEI)-modified silicon wafer. The superposition of AFM images taken at the center of both layers is shown in **Figure 1a**. The computational analysis of the AFM images using OrientationJ, an ImageJ plug-in (see Experimental Section), allowed the determination of the structure tensor for each pixel (Figure 1b) and the extraction of the pixel orientation distribution (Figure 1c). The degree of alignment of the individual CNF layers was assessed using a 2D nematic order parameter  $S_{2D} = \langle 2\cos^2\theta - 1 \rangle$ , weighted over the distribution of the angle  $\theta$  between the principal axis of the nanofibrils and the spraying direction. The values obtained for the first and second CNF layers were 0.85 and 0.80, respectively, on a scale from 0 to 1, indicating a high level of alignment. Results clearly show the  $90^\circ$  shift of the main direction of orientation of the nanofibrils deposited in each layer. Thus, successive CNF layers can be effectively oriented in independent directions by the GIS technique.

For the preparation of helicoidally oriented films, the spraying direction of the CNF suspension was rotated at a constant angle

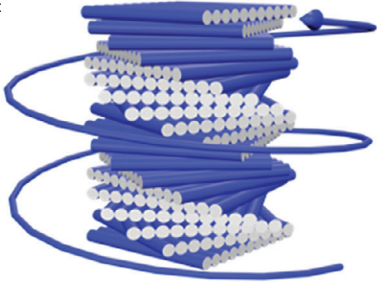
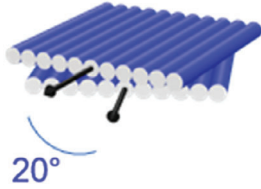
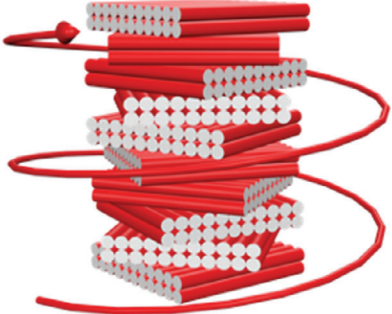
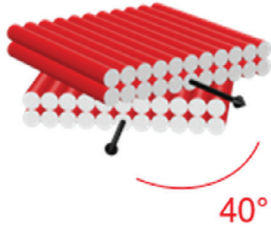
after each defined number of layers, while PVAm was used as a binder between the cellulose layers. Three main parameters were varied during the preparation of the helicoidal samples, namely, the number of successive layers of CNF sprayed in the same direction ( $S$ ), the angle ( $\alpha$ ) of in-plane rotation between successive layers or stacks of layers, and the handedness of the rotation ( $H$ ). The structural pitch ( $P$ ) is defined as the thickness observed after one complete turn ( $360^\circ$  rotation) of the helicoid; it was varied either by keeping the angle of rotation constant and changing the number of consecutive unidirectional layers, or vice versa. The nomenclature used to refer to the different samples prepared in this work is given in **Table 1**. Unless otherwise stated, all film samples were prepared with 97 CNF/PVAm layer pairs, i.e., the number of layers needed to realize four helical turns with an in-plane rotation of  $15^\circ$  between consecutive CNF layers.

The UV–visible transmittance of (PVAm/CNF)<sub>97</sub> films with different internal architectures deposited on quartz slides in the spectral range between 200 and 800 nm is reported in **Figure 2a**. The films are highly transparent with over 85%



**Figure 2.** a) Characteristic UV–visible transmittance spectra of (CNF/PVAm)<sub>97</sub> films prepared by GIS-LbL on quartz slides with different internal architectures. The spectrum of a non-oriented film prepared by dipping is shown as a reference. The inset shows a zoomed region of the spectra to highlight the presence of Fabry–Perot fringes. b) Thickness growth of different multilayer films prepared on silicon wafers followed by ellipsometry measurements. The red line represents a consolidated linear regression ( $R^2 = 0.994$ ) excluding the initial layers whose thickness growth is influenced by the substrate and is not representative of that of the bulk film.<sup>[67]</sup> The small error bars represent the standard deviation over at least five measurements made at different positions on the films.

**Table 1.** Representation of the parameters varied to modify the helical structure of the samples and of the nomenclature used to describe the prepared samples. The blue structure corresponds to a left-handed film composed of 19 CNF layers and prepared with a 20° rotation after each single CNF layer (noted 19L1 × 20°), while the red structure represents a right-handed film composed of 20 layers and assembled with a 40° rotation after two consecutive CNF layers (noted 20R2 × 40°). Both structures have the same pitch.

Helicoidal structure	# of CNF layers [L]	Handedness [H]	Unidirectional stacking [s]	Angle between rotations [ $\alpha$ ]	Nomenclature [L H S × $\alpha$ ]
Left 	19	Clockwise = Left (L)	Single (1)	 20°	19L1 × 20°
Right 	20	Counter-clockwise = Right (R)	Double (2)	 40°	20R2 × 40°

transmittance across the entire visible spectrum, while strongly absorbing UV below 250 nm. Note that slight differences in transmittance between samples are attributed to variations in the quality of the films, which is sensitive to small variations in the fabrication parameters, purity of the solutions/suspensions, quality of the compressed air, operator, etc. In contrast to helicoidal CNF films, chiral CNC-based films show a main extinction peak in the visible range corresponding to the selective reflection of the helicoidal structure.<sup>[19]</sup> Since the CNF-based films did not absorb light in the visible range, it was not possible to quantify their thickness by directly applying the Beer–Lambert law to the absorption spectra. However, Fabry–Perot fringes resulting from the interference between light reflected at the film–air and the film–substrate interfaces were detected in the highly transparent samples (as better seen in the inset of Figure 2a). This allowed the determination of the film thicknesses according to:<sup>[65,66]</sup>

$$\frac{1}{2nl} = \frac{1}{\lambda_p} - \frac{1}{\lambda_{p+1}} \quad (1)$$

where  $n$  is the average refractive index of the film (assumed to be 1.559 as in the ellipsometry measurements),  $l$  is the film thickness, and  $\lambda_p$  and  $\lambda_{p+1}$  are the wavelengths of adjacent transmission maxima. The helicoidal samples were found to be about  $1060 \pm 60$  nm thick, averaged from all the detected fringes. This value is in good agreement with the average thickness value

( $1000 \pm 100$  nm) estimated from cross-sectional SEM images (see Figure S1, Supporting Information).

The growth of the films was followed by ellipsometry on selected identical films prepared on silicon wafers. It was found that the film thickness increased regularly with the number of layer pairs and that the thickness increase was independent of the spraying direction of the layers (Figure 2b). When the films reached about 60 layer pairs, the ellipsometry data could no longer be fitted to the optical model of a single layer with a constant refractive index and varying thickness. Therefore, the thickness of thicker films was approximated by extrapolation of the consolidated linear regression of the data. In this way, the 97-layer films were estimated to be  $870 \pm 10$  nm thick. Note that this value is slightly lower than that obtained from the Fabry–Perot fringes and cross-sectional SEM. We believe that the difference may be due to the uncertainty associated either with the use of data obtained from films deposited on different substrates or with the omission of a spectral variation of the refractive index in the case of the calculation from the Fabry–Perot fringes. For practical purposes, we consider the thickness of the 97-layer pair films to be 1  $\mu\text{m}$  (the average value from the three methods being 977 nm).

Typically, thick helicoidal samples prepared by GIS-LbL exhibit a concentric pattern of colors resulting from constructive and destructive interferences of light reflected from the film–air and substrate–film interfaces, and are related to the local film thickness and the wavelength of the light through Bragg’s law.

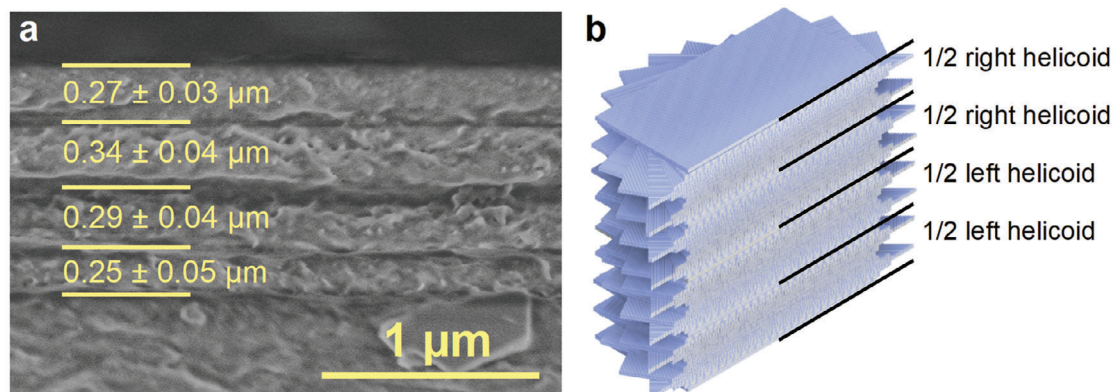


**Figure 3.** a) Cross-sectional SEM image of the helicoidal sample showing a 4-layer structure corresponding to four half-pitches of the helicoids. The thickness of these thick sub-layers was measured at multiple locations in at least six different images, and the uncertainties shown correspond to the standard deviation of the measurements. b) Cross-sectional isometric view of a 3D rendering of the twisted cross-plywood configuration of the CNFs in the prepared helicoidal film. This 3D model was prepared by stacking 10 nm thick layers of parallel cylinders following the same alignment sequence as the experimental sample.

Therefore, the homogeneity of the observed colors is commonly associated with the uniformity of the LbL film thickness.<sup>[68]</sup> The fringed color patterns of helicoidal films thus correspond to a thickness gradient that takes the form of concentric circles (Figure S2, Supporting Information).

The observation of the local orientation of the CNFs in Bouligand morphologies within the chiral materials is typically carried out by cross-sectional SEM analysis.<sup>[69]</sup> The twisting of the helicoidal orientation of the CNFs in the GIS-LbL assembled films was thus investigated by cross-sectional SEM. Since this structural pattern could not be observed in mechanically fractured samples, a sample with one right-handed helicoidal turn superimposed on one left-handed turn was sprayed on top of a non-oriented film prepared by dipping (to increase the total thickness). It was treated to obtain a brittle fracture of the film without distortion of the internal structure (see Experimental Section). A theoretical pitch of 500 nm was achieved by rotating the spraying direction by 15° after every two unidirectionally sprayed CNF layers. A representative SEM image of the cross-section of the film is shown in Figure 3a. The small diameter of the nanofibrils (1–2 nm) and possibly the high degree of hydration of the cellulose-based film prevented direct observation of a possible twist pattern of the CNFs. However, a 4-layered structure was easily discernible in all images, the number and dimensions of which correspond to the half-pitch of the helicoid, as schematically depicted in Figure 3b. This stratification is caused by the different fracture behavior of the periodic layers aligned parallel to the fracture plane compared to the layers aligned in any other direction, and it is thus an indirect evidence of the achievement of the desired characteristics of helicoidal alignment of the CNFs.

## 2.2. Optical Characterization of the Helicoidally Structured CNF-Based Films

The chiral properties induced by the helicoidal alignment of CNFs in the GIS-LbL assembled films were investigated using CD spectroscopy, an optical characterization method that measures the difference in the absorption of left and right circu-

larly polarized light of chiral substances. This non-destructive optical method is indeed typically used to prove the formation of left-handed CNC-based assemblies, the only chiral structures generated by spontaneous self-assembly of CNCs due to the homochirality in nature.<sup>[70,71]</sup> The CD signal observed for these left-handed materials exhibits a single positive broad peak in the visible spectral range corresponding to the helicoidal arrangement of the CNCs. Therefore, we relied on this method to demonstrate the internal helicoidal structure achieved in the GIS-LbL films and to investigate the resulting optical behavior.

Figure 4a shows the CD spectra obtained for two films whose only structural difference is the opposite handedness of the helicoidal alignment of the CNFs. For comparison, the spectrum measured for a non-oriented control sample is also plotted. The latter in-plane isotropic film showed no significant CD signal except for a weak positive response around 220 nm corresponding to the individual components (see Figure S3, Supporting Information). The most noticeable feature of the spectra is the opposite chirality of the GIS-structured films prepared with opposite handedness, confirming the effective helicoidal assembly of the CNF within the films.

Contrary to left-handed CNC assemblies showing only a single positive peak,<sup>[19,34]</sup> CD spectra of CNF-based films exhibit both positive and negative peaks at different wavelengths, changing sign around 230 nm, i.e., at the onset of the signal of the individual components. Moreover the transmittance of UV light by the oriented cellulose films is low (see transmittance spectra in Figure 2a), therefore the smaller peaks at around 220 nm correspond to the combined effect of many absorption, scattering and reflection processes, including those of helicoidal assembly of oriented nanofibers and the absorbance of the individual components (Figure S9, Supporting Information). Analysis of the CD spectra of non-oriented and oriented samples underlines that the contribution of the individual components to the CD signal in the UV region is negligible compared to those of the helicoidally structured films, indicating that the CD signal observed in the UV region comes from the chiral arrangement of the CNFs.

CD spectra of the chiral structures show three characteristic peaks: a broad and intense peak at around 390 nm, a

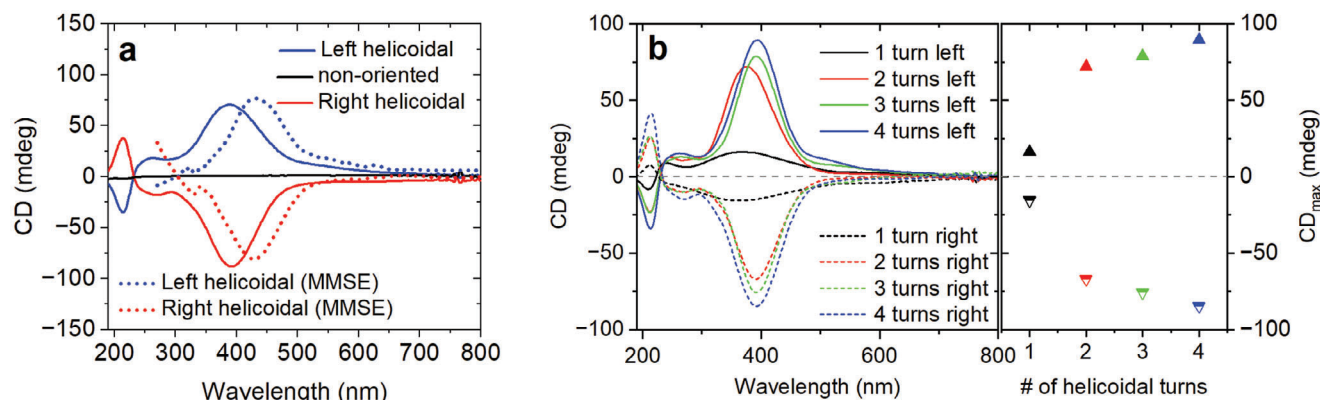


**Figure 4.** a) CD spectra of right- and left-handed helical films (samples 97R1  $\times$  15° and 97L1  $\times$  15°, respectively). The dotted curves are the CD spectra extracted from MMSE to verify that the signals from CD spectroscopy are not due to artifacts, as might be the case for samples with linear anisotropies.<sup>[75,76]</sup> We observed that the sign, shape, and magnitude of the CD signals obtained were comparable in both techniques, with only the position of the peaks being consistently blue-shifted ( $40 \pm 7$  nm in all samples) when measured by CD spectroscopy. This shift in the CD signals might be due to changes in the pitch caused by the swelling of the film due to differences in the ambient humidity. See more data from MMSE in Figures S4–S6 (Supporting Information). b) CD spectra collected after the completion of different numbers of helical turns during the assembly of 97R2  $\times$  30° and 97L2  $\times$  30° samples. The right panel shows the intensity of the structural peak at  $\approx 390$  nm as a function of the number of helical turns.

shoulder at about 260 nm, and a smaller peak of opposite sign at around 220 nm. The broad and intense CD peak which was not present in the spectra of the individual components can be assigned to the structural arrangement of the CNFs corresponding to the Bragg reflection peak typically observed for helicaloidal CNC assemblies.<sup>[19,34]</sup> The shoulder and the smaller opposite peak, not observed in chiral CNC materials, originate probably from the overlapping of the CD band corresponding the Bragg reflection band with a bisignated CD band in the UV (i.e., the CD changes locally in sign) coming from the absorption of the constitutive materials located in each anisotropic layer. Bisignated CD signals are typically resulting from an anisotropic absorption of the material. Indeed, the chiral material can support two slightly shifted absorption bands: one for the right-handed and another one for the left-handed.<sup>[72,73]</sup> Simulations were performed to understand the origin of the bisignated CD peak observed in the material exhibiting an absorption band in this spectral range. The cellulose material was described by a Lorentzian oscillator (see Section 3 in the Supporting Information). The simulated CD spectra of the structure (Figure S9d, Supporting Information) reproduces the bisignated CD band in UV. This result suggests that the CD signal observed in the 200–300 nm spectral range comes from the absorption of the constitutive materials located in each layer. Such bisignated CD band is not observed for chiral CNC assemblies as they display negligible absorption in UV.

The positive signal of the left-handed helical film indicates that L-CPL is reflected to a greater extent than R-CPL, i.e., circularly polarized light with the same handedness as the cholesteric structure of the film is preferentially reflected, while the opposite handedness is transmitted, as observed for the circular Bragg phenomenon.<sup>[74]</sup> The same observation applies to the negative CD signal measured in the right-handed sample. The selective Bragg reflection at normal incidence takes place in a spectral band centered at  $k \lambda_{\text{Bragg}} = \bar{n} P$ , where  $\bar{n}$  is the in-plane average refractive index,  $P$  is the helix pitch, and  $k$  is an integer indicating the order of each maximum. Assuming  $\bar{n} = 1.559$  and  $P \approx 1 \mu\text{m}/4 \text{ turns} \approx 250$  nm, we estimated a wavelength of selec-

tive Bragg reflection ( $k = 1$ ) located at  $\approx 390$  nm, which is in good agreement with the structural CD peak at 390 nm.

The intensity of the structural CD peaks was  $\approx 80$  mdeg, corresponding to a g-factor of  $\approx 0.013$  (Figure S10, Supporting Information), which represents a 0.2% efficiency in filtering circular polarization (defined as the ellipticity achieved relative to perfect circular polarization, i.e., 45000 mdeg). Since the CD signal is based on the measurement of light transmitted through the sample, its intensity is related to the concentration of the attenuating species (Beer's law) when measured for chiral molecules in solution. In the case of chiral structured films, the intensity of the structural CD peak must depend mostly on the number of helical turns rather than on the actual concentration of CNFs, as evidenced by the absence of CD signals in the spectrum of the non-oriented control film of the same thickness (Figure 4a). Figure 4b shows the effective monotonic increase in the intensity of the structural CD peak with the increasing number of helical turns. However, as the variation of the CD and of the extinction is not linear with the number of turns, the g-factor spectrum of the 2-turn sample is higher and reaches a maximum value of 0.032 (Figure S11, Supporting Information). The CD intensity measured after only one turn was weak, possibly because the film thickness at this stage ( $\approx 240$  nm) was thinner than  $\lambda_{\text{Bragg}}$ . Note that the intensity of the smaller CD peaks at around 220 nm follows the same trend, confirming that these CD signals originate from the effective helicaloidal assembly of the CNF within the films (taking into account the negligible CD contribution of individual components).

Left-handed helicaloidal films prepared with estimated pitches of 80 nm (12 helical turns), 245 nm (4 helical turns), and 490 nm (2 helical turns) were also investigated by CD spectroscopy (Figure 5a). We observed a red shift in the position of the broad structural peak with increasing pitch, as predicted by Bragg's law (Figure 5c), and an intensity increase of the CD peak in the UV region with increasing pitch. Note that the signal corresponding to the film with the smallest pitch overlaps with the negative peak observed for all CNF films at around 220 nm. The

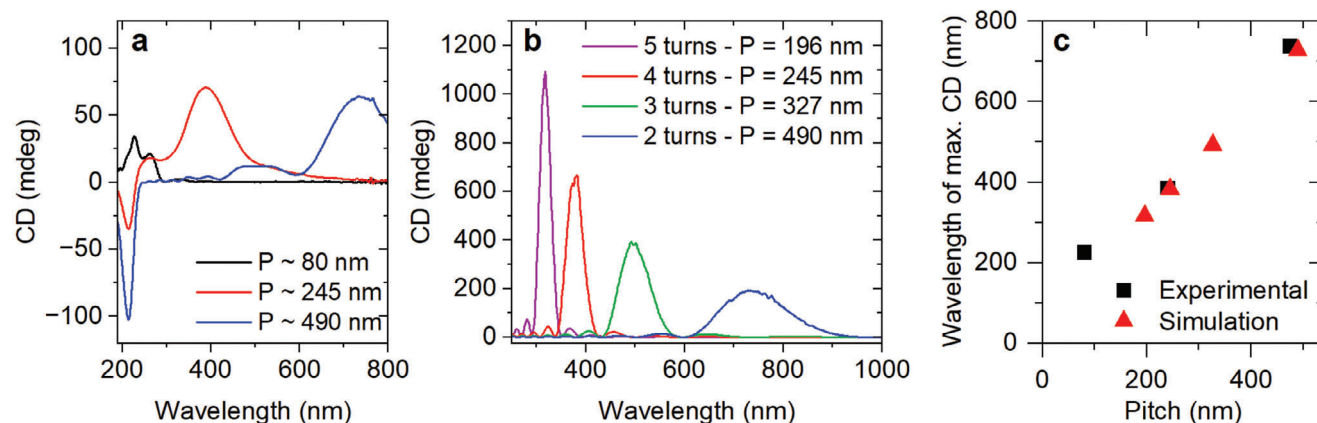


**Figure 5.** a) *CD* spectra of three left-handed films with different helical pitch. b) Simulated *CD* spectra of left-handed films with an increasing number of helical turns at a fixed film thickness, resulting in a decrease in the helical pitch. c) Linear relationship between the helical pitch and the position of the resulting structural *CD* peak (the dashed line is an eye guide).

intensity and sign change of the peak at 220 nm with decreasing pitch can be explained by the shift of the positive Bragg reflection band to lower wavelength leading to an increasing overlap with the bisignated *CD* absorption band. This overlap is maximum for a pitch of 80 nm for which the resulting *CD* signal is positive. Apart from their position, the broad peaks seemed to broaden as they moved to higher wavelengths.

To verify this behavior, the *CD* spectra of helicoidal films with different pitches were numerically simulated using the Berreman transfer matrix formalism.<sup>[77,78]</sup> This was accomplished by modeling films composed of a stack of uniaxial anisotropic layers with an increasing number of helicoidal turns while keeping the thickness constant. The theoretical modeling corroborated the experimental observations of a linear red-shift of the broad *CD* peak with the increasing pitch of the helicoidal arrangement of the nanofibrils (Figure 5b,c), confirming the structural nature of the signal. However, the intensities of the structural peaks obtained by the simulation were considerably higher than the experimental values. The reasons may be related to the idealization of the model, which considers homogeneous birefringent layers of identical composition and thickness. Moreover, the ordinary and extraordinary refractive indices determined on a 120 nm thick film (Figure S7, Supporting Information) may not represent the actual optical properties of the  $\approx 10$  nm thick unidirectional layers that form the experimental helical stacks. Nevertheless, since the modeled films had the same thickness, the simulation also allowed us to verify that the intensity of the *CD* peak is not related to the actual thickness of the sample but is mainly a function of the number of helical turns, increasing monotonically with this parameter, as discussed above. The *CD* band in UV observed in the measured spectra is not reproduced in this simulation. Indeed, as shown in the SI, this band is attributed to the UV absorption of each layer. In the simulation presented in the Figure 5b, we do not consider this absorption since the optical constant are only measured in the transparent spectral range (270–1000 nm).

The qualitative agreement between the simulations and the experimental measurements of the polarization properties of helicoidally structured (CNF/PVAm)<sub>n</sub> films indicates that tailored optical behaviors can be easily designed theoretically before engag-

ing in the time-consuming fabrication of the films by GIS-LbL. We have identified relevant parameters to design films with the desired optical behavior. In particular, the localization of the selective Bragg reflection peak can be tuned by choosing the appropriate helical pitch, while the handedness of the selective transmission is determined by the choice of the handedness of the chiral structure. Broadband wave filtration could be achieved by stacking helicoids with different pitches. Finally, the efficiency of selective filtration of circularly polarized light increases with the number of helicoidal turns. A film thickness of around several tens of micrometers would be required for narrowband filtration and even thicker films, for broadband functionality. However, there is much room for optimization in our approach. As illustrated in Figure S8 (Supporting Information), the amplitude of the simulated *CD* band increases with the birefringence of each layer. Indeed, this birefringence combined with the helical structure is responsible for the *CD* signal, it can be tuned by controlling the volume fraction and the order parameter of the cellulose nanofibrils. Thus, the use of wider and less flexible nanoparticles such as cellulose nanocrystals (around ten times wider than CNF) would reduce the number of layers required and improve the birefringence in each layer, thereby increasing the circular dichroism of the films as predicted by our simulations. Of course the penalty of using CNC (or other wider nano-rods) would be that the individual layers would be thicker and the control of the architecture along the layer normal would become more coarse.

### 3. Conclusion

We demonstrate that the combination of layer-by-layer assembly, which allows one to control the sequence of deposited materials, and grazing incidence spraying, by which provides a unidirectional alignment in each layer, is an effective approach to constructing multilayer films with tuned helicoidal architectures. Nanocomposite films with the desired Bouligand architecture were successfully prepared, as confirmed by cross-sectional SEM, *CD* spectroscopy, and MMSE.

The handedness and pitches of the helicoidal arrangement of the CNFs were varied by the rationally selecting the spraying



direction, the angle of in-plane rotation between layer stacks, and the number of layers oriented in the same direction. A characteristic of such structured thin films is the circular Bragg reflection phenomenon, in which circularly polarized light with the same handedness as the chiral structure of the film is preferentially reflected, while the opposite handedness is transmitted. This behavior was confirmed by the strong *CD* peak detected in all helical samples, approximately centered at a wavelength proportional to the average in-plane refractive index of the film and the pitch of the chiral structure, thus providing evidence of the structural nature of the signal.

The present study lays the groundwork for the preparation of nanocomposite films with well-controlled internal structures of the reinforcing fibrillar phase, which can be exploited to impart enhanced mechanical and optical functionalities to the resulting films. We have worked with cellulose nanofibrils, a material with a promising application as an environmentally friendly alternative to petroleum-based raw materials, but the additive fabrication route presented in this work can be easily transferred to other nanofibrillar components, such as cellulose nanocrystals, to increase the efficiency in the filtration of circularly polarized light.

We note that while other fabrication routes (e.g., EISA),<sup>[33]</sup> which are faster and applicable to larger areas, are increasingly being used to prepare chiral CNC films, the GIS-LbL method offers more choice for tuning layer composition, structure and overall architecture. Indeed, such control is a major advantage of our strategy, which enables the preparation of organized structures of unprecedented complexity. For example, it offers the possibility to incorporate various sub-structures within the same film, such as the combination of opposite handedness of the chiral assembly, the alternation with unidirectional segments, or the staking of different pitches to tune the optical response of the material. In addition, the versatility, robustness, and industrial viability of the LbL technology offer many opportunities for improvement, optimization, and scale-up. For instance, it is based on a simple and commercially available industrial spraying technology, so that the programming of the spraying sequence utilizing robotic arms can be used to prepare large-area devices.

The approach developed in this work paves the way for the preparation of innovative damage-resistant<sup>[10–16]</sup> optical filtering thin films with well-defined composition, structures, and properties, and will generate unique advanced applications of nanotechnology in materials science. Such multifunctional bio-based composite materials will be competitive for future applications (e.g., high-performance composites, protective coatings, optical filters, flexible displays) and will address the environmental and societal needs for non-petroleum-based sustainable high-performance products.

## 4. Experimental Section

**Materials:** Carboxymethylated nanofibrillated cellulose (degree of substitution of 0.087) was provided as a pulp containing 2.26 wt% concentration in water by Innventia AB (Stockholm, Sweden). The pulp was mechanically dispersed in Milli-Q water (Milli-Q Advantage A10 water purification system, Merck-Millipore, Molsheim, France) to obtain a suspension at 2 g L<sup>-1</sup> and sonicated with a sonic dismembrator model 505 (Fischer Scientific, USA) for 20 min at 30% amplitude. The suspension was then centrifuged for 1 h at 9500 rpm in a ROTINA 420R centrifuge (Hettich Zentrifugen, Germany). The resulting supernatant was first filtered on cotton

wool and then through a 5 μm PVDF syringe filter Millex-SV (Merck, Germany). The final concentration was typically 1.4 g L<sup>-1</sup> as determined from dry mass measurements.

Poly(vinyl amine) (PVAm, trade name Lupamin 9095, 20% in water,  $\overline{M}_w \approx 340\,000$  g mol<sup>-1</sup>) provided by BASF (Ludwigshafen, Germany) was used to prepare solutions at a concentration of 1 g L<sup>-1</sup> and their pH was adjusted at 8 with a solution of 0.5 M NaOH. Poly(ethylene imine) (PEI, 50 wt% in water,  $\overline{M}_w \approx 750\,000$  g mol<sup>-1</sup>) purchased from Sigma-Aldrich (Lyon, France) was dissolved in Milli-Q water under bath sonication to a final concentration of 2.5 g L<sup>-1</sup>.

(100)-silicon wafers used as substrates were obtained from WaferNet, Inc. (San Jose, CA, USA). Quartz slides (25 mm × 25 mm × 1 mm) were acquired from Agar Scientific Ltd. (Stansted, UK).

**Substrate Preparation:** The silicon wafers and quartz slides were cleaned in a 50:50 solution (V/V) of Milli-Q water:ethanol and sonicated for 15 min in an ultrasound bath, after which they were blown dried with non-fatty compressed air and finally, cleaned/activated by 3 min plasma treatment in a plasma cleaner PDC-002 (Harrick Plasma, USA) at a high RF power (≈30 W).

**GIS-LbL Deposition:** All films were deposited on a substrate (silicon or quartz) coated with a precursor layer of PEI. Alternated layers of CNF and PVAm were sprayed using intermediate rinsing steps with Milli-Q water. GIS deposition was performed semi-automatically with the help of a spraying system made in-house (Figure S12, Supporting Information). The colloidal suspension of CNFs was pumped using a liquid handling pump (model M50, VICI AG, Schenkon, Switzerland) into a stainless-steel air atomizing nozzle (Spraying Systems Co., Glendale Heights, IL, USA), which was likewise supplied with non-fatty compressed air controlled by a gas flow controller Red-y (Vögtlin Instruments GmbH, Aesch, Switzerland). The sample was kept in a vertical position using a rubber stopper and a pulling vacuum. The spraying direction was always pointing vertically downward and the angle of the nozzle to the substrate surface was kept fixed at 10°. The liquid flow rate was set to 1 mL min<sup>-1</sup>, the airflow rate to 40 L min<sup>-1</sup>, and the spraying time to 60 s. The PVAm solution and rinsing water were sprayed manually (orthogonal to the substrate) for 5 and 10 s, respectively, with AIR-BOY spray bottles (Carl Roth GmbH, Karlsruhe, Germany).

A control sample in which the nanofibrils were deposited without any preferential orientation was prepared by dip-assisted LbL. The plasma-activated substrate was alternately immersed in beakers containing either the polycation solution or the CNF suspension for 10 min followed by three intermediate rinsing steps of 1 min each in Milli-Q water and a drying step with non-fatty compressed air.

**Atomic Force Microscopy:** Tapping mode atomic force microscopy was performed on a Bruker AFM Dimension Icon (Bruker, USA) with a Nanoscope V controller and silicon cantilevers (resonance frequency 300 kHz, nominal spring constant of 42 N m<sup>-1</sup>, and nominal tip radius of 7 nm). Phase and height imaging channels were recorded simultaneously using a scan rate of 1.0 Hz with a resolution of 512 × 512 pixels<sup>2</sup>.

**Orientation Analysis:** The distribution of the angle  $\theta$  between the principal axis of the nanofibrils and the spraying direction was extracted from the AFM images using the directional image analysis plug-in OrientationJ<sup>[79]</sup> (Biomedical Imaging Group, EPFL, Switzerland) developed for ImageJ. This method is based on the analysis of the local structure tensor in the local neighborhood of each pixel of the image. As a result, the angle of orientation of every pixel is calculated and represented as a given color, while the angle distribution can be also extracted. A complete description of the principle of operation of the plug-in can be found elsewhere.<sup>[62]</sup>

**Scanning Electron Microscopy:** To image the internal structure of multilayer films, the supported sample was first crosslinked by dipping into a glutaraldehyde (GA) solution (5% in H<sub>2</sub>O) for two hours before being rinsed in Milli-Q water for 5 min. Then, the film was subjected to dehydration by dipping it sequentially into ethanol/water solutions with increasing concentrations of the alcohol (25%, 50%, 75%, and 100%) for 10 min each time. Immediately after, the film was carefully fractured inside liquid N<sub>2</sub>, dipped once more in the GA solution to crosslink the exposed cross-section, and rinsed in Milli-Q water for 5 min. This procedure was adopted

to try to obtain a brittle fracture of the film without distortion of the internal structure. The sample was glued vertically to a cross-section holder using conductive carbon cement Leit-C (Agar Scientific, UK) and imaged with a Field Emission Gun Scanning Electron Microscope (FEG-SEM) SU8010 (Hitachi, Japan) with a secondary electron detector at an accelerating voltage of 1 kV.

The total thickness of samples was determined on film that were fractured mechanically and then glued vertically on a cross-section holder using carbon cement. The sample cross-section was observed using a FE-SEM Hitachi SU8010 at 3 kV. The images were taken with the SE-in lens detector.

**Spectroscopic Ellipsometry:** The thickness of samples deposited on silicon wafers was measured on a spectroscopic ellipsometer SENpro (SENTECH Instruments GmbH, Germany) and its built-in software SENpro 1.2.4. The ( $\psi$ ,  $\Delta$ ) spectra were obtained in the spectral range between 400 and 800 nm using an incident angle of 70°. The deposited film was approximated to an effective medium with a homogeneous refractive index  $n = 1.559$ , as previously done by others in the group for CNF-based multilayer films.<sup>[80]</sup> The thickness of the films was followed as a function of the number of layer pairs and the linear regression of the data was used to estimate the thickness of the thicker films. The root-mean-square error (RMSE) was used as the uncertainty of the predicted data.

**Mueller Matrix Spectroscopic Ellipsometry:** Transmission Mueller matrix measurements were performed with a spectroscopic ellipsometer UVISEL (HORIBA, Japan) at normal incidence in the spectral range 270–800 nm (limits of the equipment). The beam diameter is about 0.8 mm. This ellipsometer only allows determining the first three columns of the Mueller matrix, the last column can be obtained by symmetry provided that the depolarization of the sample is negligible. This was verified using a dual rotating retarder compensator ellipsometer in the spectral range 380–800 nm. The beam diameter of the dual rotating compensator ellipsometer is 1 mm.

**Numerical Simulation:** The optical transmittance behavior of the helicoidal samples was numerically simulated through the Berreman transfer matrix formalism.<sup>[77,78]</sup> Films were modeled as a stack of 97 unidirectional layers constantly rotated by a fixed azimuth angle. Each 10 nm layer was considered as having homogeneous anisotropic optical parameters defined in Figure S7 (Supporting Information). These indices were determined by fitting the reflection Mueller matrix measured at different azimuth angles on a 120 nm thick unidirectional film prepared on a silicon wafer by GIS-LbL.

**UV-Vis and CD Spectroscopy:** Transmittance spectra of LbL films deposited on quartz slides were recorded on a Cary 5000 UV-vis-NIR spectrometer (Agilent Technologies, Inc., USA) in the spectral range between 200 and 800 nm. CD spectra were measured with a Jasco J-1700 circular dichroism spectrometer equipped with a xenon arc lamp.

## Supporting Information

Supporting Information is available from the Wiley Online Library or from the author.

## Acknowledgements

The authors acknowledge the Ministère de l'Enseignement Supérieur, de la Recherche et de l'Innovation (MESRI, France), the Centre National de la Recherche Scientifique (CNRS, France), and the International Center for Frontier Research in Chemistry (IcFRC, France) for their support. They also express their gratitude to Christophe Contal (ICS, France) and Mircea Rastei (IPCMS, France) for the AFM training, to the characterization platform of ICS for the UV-vis measurements and to the Electron Microscopy platform of ICS for SEM imaging, to Innventia AB (Sweden) for supplying CNFs, and to BASF (Germany) for supplying PVAm. The authors thank the Ellipsometry core facility of LCP-A2MC (Université de Lorraine, <http://lcp-a2mc.univ-lorraine.fr>).

## Conflict of Interest

The authors declare no conflict of interest.

## Data Availability Statement

The data that support the findings of this study are available from the corresponding author upon reasonable request.

## Keywords

bouligand architecture, chiroptical properties, helicoidal nanostructured films, layer-by-layer assembly, nanocellulose, nanocomposite thin films, spray-assisted alignment

Received: February 1, 2024

Revised: April 5, 2024

Published online:

- [1] M. A. Meyers, P.-Y. Chen, A. Y.-M. Lin, Y. Seki, *Prog. Mater. Sci.* **2008**, 53, 1.
- [2] U. G. K. Wegst, H. Bai, E. Saiz, A. P. Tomsia, R. O. Ritchie, *Nat. Mater.* **2015**, 14, 23
- [3] S. E. Naleway, M. M. Porter, J. McKittrick, M. A. Meyers, *Adv. Mater.* **2015**, 27, 5455.
- [4] W. Zhang, J. Xu, T. X. Yu, *Eng. Struct.* **2022**, 265, 114490.
- [5] D. Nepal, S. Kang, K. M. Adstedt, K. Kanhaiya, M. R. Bockstaller, L. C. Brinson, M. J. Buehler, P. V. Coveney, K. Dayal, J. A. El-Awady, L. C. Henderson, D. L. Kaplan, S. Keten, N. A. Kotov, G. C. Schatz, S. Vignolini, F. Vollrath, Y. Wang, B. I. Yakobson, V. V. Tsukruk, H. Heinz, *Nat. Mater.* **2023**, 22, 18.
- [6] M. A. Meyers, A. Y. M. Lin, Y. Seki, P. Y. Chen, B. K. Kad, S. Bodde, *J. Osteopath. Med.* **2006**, 58, 35.
- [7] S. Ling, D. L. Kaplan, M. J. Buehler, *Nat. Rev. Mater.* **2018**, 3, 18016
- [8] A. C. Neville, B. M. Luke, *Tissue Cell* **1969**, 1, 689.
- [9] S. M. Chen, S. M. Wen, S. C. Zhang, C. X. Wang, S. H. Yu, *Matter* **2024**, 7, 378.
- [10] D. Raabe, C. Sachs, P. Romano, *Acta Mater.* **2005**, 53, 4281.
- [11] S. Nikolov, M. Petrov, L. Lympirakis, M. Friák, C. Sachs, H. O. Fabritius, D. Raabe, J. Neugebauer, *Adv. Mater.* **2010**, 22, 519.
- [12] W. Yang, V. R. Sherman, B. Gludovatz, M. Mackey, E. A. Zimmermann, E. H. Chang, E. Schaible, Z. Qin, M. J. Buehler, R. O. Ritchie, M. A. Meyers, *Acta Biomater.* **2014**, 10, 3599.
- [13] P.-Y. Chen, A. Y.-M. Lin, J. McKittrick, M. A. Meyers, *Acta Biomater.* **2008**, 4, 587.
- [14] J. C. Weaver, G. W. Milliron, A. Miserez, K. Evans-Lutterodt, S. Herrera, I. Gallana, W. J. Mershon, B. Swanson, P. Zavattieri, E. DiMasi, D. Kisailus, *Science* **2012**, 336, 1275.
- [15] A. C. Neville, S. Levy, *Planta* **1984**, 162, 370.
- [16] J. Plocher, L. Mencattelli, F. Narducci, S. Pinho, *Compos. Sci. Technol.* **2021**, 208, 108669.
- [17] H. Arwin, T. Berlind, B. Johs, K. Järrendahl, *Opt. Express* **2013**, 21, 22645.
- [18] L. Fernández Del Río, H. Arwin, K. Järrendahl, *Thin Solid Films* **2014**, 571, 410.
- [19] B. Frka-Petesic, T. G. Parton, C. Honorato-Rios, A. Narkevicius, K. Ballu, Q. Shen, Z. Lu, Y. Ogawa, J. S. Haataja, B. E. Droguet, R. M. Parker, S. Vignolini, *Chem. Rev.* **2023**, 123, 12595.
- [20] J. P. Vigneron, P. Simonis, *Phys. B* **2012**, 407, 4032.
- [21] H. P. Meyers, *Introductory Solid State Physics*, 2nd ed., CRC press, London, **1997**.

- [22] S. Vignolini, P. J. Rudall, A. V. Rowland, A. Reed, E. Moyroud, R. B. Faden, J. J. Baumberg, B. J. Glover, U. Steiner, *Proc. Natl. Acad. Sci. U. S. A.* **2012**, *109*, 15712.
- [23] S. Vignolini, T. Gregory, M. Kolle, A. Lethbridge, E. Moyroud, U. Steiner, B. J. Glover, P. Vukusic, P. J. Rudall, *J. R. Soc., Interface* **2016**, *13*, 20160645.
- [24] A. C. Neville, S. Caveney, *Biol. Rev. Cambridge Philos. Soc.* **1969**, *45*, 531.
- [25] V. Sharma, M. Crne, J. O. Park, M. Srinivasarao, *Mater. Today Proc.* **2014**, *1*, 161.
- [26] S. Berthier, M. Thomé, P. Simonis, *Mater. Today Proc.* **2014**, *1*, 145.
- [27] I. E. Carter, K. Weir, M. W. McCall, A. R. Parker, *J. R. Soc., Interface* **2016**, *13*, 20160015.
- [28] L. T. McDonald, E. D. Finlayson, B. D. Wilts, P. Vukusic, *Interface Focus* **2017**, *7*, 20160129.
- [29] S. Caveney, *Proc. R. Soc. London, Ser. B* **1971**, *178*, 205.
- [30] Z. Han, F. Wang, J. Sun, X. Wang, Z. Tang, *Adv. Mater.* **2023**, *35*, 2206141.
- [31] J. Lv, D. Ding, X. Yang, K. Hou, X. Miao, D. Wang, B. Kou, L. Huang, Z. Tang, *Angew. Chem., Int. Ed.* **2019**, *58*, 7783.
- [32] Y. Yang, Z. Chen, X. Song, Z. Zhang, J. Zhang, K. K. Shung, Q. Zhou, Y. Chen, *Adv. Mater.* **2017**, *29*, 1605750.
- [33] S. M. Parkab, D. K. Yoon, *Mater. Horiz.* **2024**, *11*, 1843.
- [34] D. Bukharina, R. Xiong, M. Kim, X. Zhang, S. Kang, V. V. Tsukruk, *Liq. Cryst.* **2023**, *50*, 121.
- [35] J.-F. Revol, H. Bradford, J. Giasson, R. H. Marchessault, D. G. Gray, *Int. J. Biol. Macromol.* **1992**, *14*, 170.
- [36] J.-F. Revol, D. L. Godbout, D. G. Gray, US 5629065, **1997**.
- [37] Z. Yu, K. Wang, X. Lu, *Int. J. Biol. Macromol.* **2021**, *188*, 385.
- [38] Y. Meng, Y. Cao, H. Ji, J. Chen, Z. He, Z. Long, C. Dong, *Carbohydr. Polym.* **2020**, *240*, 16281.
- [39] W. Fan, J. Li, L. Wei, Y. Xu, *Carbohydr. Polym.* **2022**, *289*, 119442.
- [40] M. Xu, W. Li, C. Ma, H. Yu, Y. Wu, Y. Wang, Z. Chen, J. Li, S. Liu, *J. Mater. Chem.* **2018**, *6*, 5391.
- [41] R. S. Lodhi, P. Das, *ACS Appl. Nano Mater.* **2023**, *6*, 16580.
- [42] X. Zhang, R. Xiong, S. Kang, Y. Yang, V. V. Tsukruk, *ACS Nano* **2020**, *14*, 14675.
- [43] V. Sharma, M. Crne, J. O. Park, M. Srinivasarao, *Science* **2009**, *325*, 449.
- [44] B. R. Harkness, D. G. Gray, *Can. J. Chem.* **1990**, *68*, 1135.
- [45] J. Pan, W. Hamad, S. K. Straus, *Macromolecules* **2010**, *43*, 3851.
- [46] B. Frka-Petesic, G. Guidetti, G. Kamita, S. Vignolini, *Adv. Mater.* **2017**, *29*, 1701469.
- [47] Y. Habibi, T. Heim, R. Douillard, *J. Polym. Sci., Part B: Polym. Phys.* **2008**, *46*, 1430.
- [48] S. N. Fernandes, P. L. Almeida, N. Monge, L. E. Aguirre, D. Reis, C. L. P. de Oliveira, A. M. F. Neto, P. Pieranski, M. H. Godinho, *Adv. Mater.* **2017**, *29*, 1603560.
- [49] J. Tao, C. Zou, H. Jiang, M. Li, D. Lu, S. Mann, Y. Xu, *CCS Chem.* **2021**, *3*, 932.
- [50] S. Beck, J. Bouchard, G. Chauve, R. Berry, *Cellulose* **2013**, *20*, 1401.
- [51] A. G. Dumanli, G. Kamita, J. Landman, H. van der Kooij, B. J. Glover, J. J. Baumberg, U. Steiner, S. Vignolini, *Adv. Opt. Mater.* **2014**, *2*, 646.
- [52] A. G. Dumanli, H. M. Van Der Kooij, G. Kamita, E. Reisner, J. J. Baumberg, U. Steiner, S. Vignolini, *ACS Appl. Mater. Interfaces* **2014**, *6*, 12302.
- [53] G. Decher, J.-D. Hong, *Makromol. Chem., Macromol. Symp.* **1991**, *46*, 321.
- [54] G. Decher, Y. Lvov, J. Schmitt, *Thin Solid Films* **1994**, *244*, 772.
- [55] G. Decher, *Science* **1997**, *277*, 1232.
- [56] K. Katagiri, R. Hamasaki, K. Ariga, J. I. Kikuchi, *Langmuir* **2002**, *18*, 6709.
- [57] K. Katagiri, R. Hamasaki, K. Ariga, J.-I. Kikuchi, *J. Am. Chem. Soc.* **2002**, *124*, 7892.
- [58] Q. Ji, S. B. Yoon, J. P. Hill, A. Vinu, J. S. Yu, K. Ariga, *J. Am. Chem. Soc.* **2009**, *131*, 4220.
- [59] R. Blell, X. Lin, T. Lindström, M. Ankerfors, M. Pauly, O. Felix, G. Decher, *ACS Nano* **2017**, *11*, 84.
- [60] H. Hu, M. Pauly, O. Felix, G. Decher, *Nanoscale* **2017**, *9*, 1307.
- [61] R. Merindol, S. Diabang, R. Mujica, V. le Houerou, T. Roland, C. Gauthier, G. Decher, O. Felix, *ACS Nano* **2020**, *14*, 16525.
- [62] H. Hu, S. Sekar, W. Wu, Y. Battie, V. Lemaire, O. Arteaga, L. V. Poulikakos, D. J. Norris, H. Giessen, G. Decher, M. Pauly, *ACS Nano* **2021**, *15*, 13653.
- [63] B. Las-Casas, I. K. R. Dias, S. L. Yupanqui-Mendoza, B. Pereira, G. R. Costa, O. J. Rojas, V. Arantes, *Int. J. Biol. Macromol.* **2023**, *250*, 126007.
- [64] R. Mujica, A. Augustine, M. Pauly, V. Le Houerou, G. Decher, Y. Battie, O. Felix, *Compos. Sci. Technol.* **2023**, *233*, 109889.
- [65] S. Reculosa, S. Ravaine, *Chem. Mater.* **2003**, *15*, 598.
- [66] Y. Guan, S. Yang, Y. Zhang, J. Xu, C. C. Han, N. A. Kotov, *J. Phys. Chem. B* **2006**, *110*, 13484.
- [67] R. A. McAloney, M. Sinyor, V. Dudnik, M. C. Goh, *Langmuir* **2001**, *17*, 6655.
- [68] L. Wågberg, G. Decher, M. Norgren, T. Lindström, M. Ankerfors, K. Axnäs, *Langmuir* **2008**, *24*, 784.
- [69] J. Majoinen, E. Kontturi, O. Ikkala, D. G. Gray, *Cellulose* **2012**, *19*, 1599.
- [70] K. E. Shopsowitz, J. A. Kelly, W. Y. Hamad, M. J. MacLachlan, *Adv. Funct. Mater.* **2014**, *24*, 327.
- [71] L. Liu, L. Wang, S. Luo, Y. Qing, N. Yan, Y. Wu, *J. Mater. Sci.* **2019**, *54*, 6699.
- [72] N. Berova, L. Di Bari, G. Pescitelli, *Chem. Soc. Rev.* **2007**, *36*, 914.
- [73] N. S. Shahana Nizar, M. Sujith, K. Swathi, C. Sissa, A. Painelli, K. G. Thomas, *Chem. Soc. Rev.* **2021**, *50*, 11208.
- [74] M. Faryad, A. Lakhtakia, *Adv. Opt. Photonics* **2014**, *6*, 225.
- [75] H. P. Jensen, J. A. Schellman, T. Troxell, *Appl. Spectrosc.* **1978**, *32*, 192.
- [76] Y. Shindo, M. Nishio, S. Maeda, *Biopolymers* **1990**, *30*, 405.
- [77] D. W. Berreman, *J. Opt. Soc. Am.* **1972**, *62*, 502.
- [78] D. W. Berreman, *J. Opt. Soc. Am.* **1973**, *63*, 1374.
- [79] R. Rezakhanliha, A. Agianniotis, J. T. C. Schrauwen, A. Griffa, D. Sage, C. V. C. Bouten, F. N. Van De Vosse, M. Unser, N. Stergiopoulos, *Biomech. Model. Mechanobiol.* **2012**, *11*, 461.
- [80] R. Merindol, S. Diabang, O. Felix, T. Roland, C. Gauthier, G. Decher, *ACS Nano* **2015**, *9*, 1127.